ACS APPLIED MATERIALS & INTERFACES

Research Article

www.acsami.org

Wet Chemical Method for Making Graphene-like Films from Carbon Black

Michela Alfè,*[,†] Valentina Gargiulo,[†] Roberto Di Capua,[‡,§] Fabio Chiarella,[⊥] Jean-Noel Rouzaud,[#] Alessandro Vergara,[∥] and Anna Ciajolo[†]

[†]Istituto di Ricerche sulla Combustione (IRC)-CNR, P.le Tecchio, 80, 80125 Napoli, Italy

[‡]SPIN-CNR UOS Napoli, via Cintia, I-80126, Napoli, Italy.

[§]Dipartimento S.pe.S., Universita' del Molise, Via De Sanctis, I-86100, Campobasso, Italy

[⊥]SPIN-CNR UOS Salerno, Via Ponte don Melillo, I-84084, Fisciano (SA), Italy

[#]Laboratoire de Geologie, Ecole Normale Superieure, 24 Rue Lhomond, 75231 Paris Cedex 05, France

[∥]Dipartimento di Scienze Chimiche, Complesso Universitario di Monte Sant'Angelo, Via Cintia, 21, 80126 Napoli, Italy

ABSTRACT: Reduction of strongly oxidized carbon black by hydrazine hydrate yields water-insoluble graphene-like sheets that undergo to self-assembling in thin film on surfaces after drying. The height of a drop-casted graphene-like film was determined by atomic force microscopy (AFM) to be around 20 nm, corresponding to approximately 25 graphene-like layers. The oxidized carbon black and the corresponding reduced form were carefully characterized.

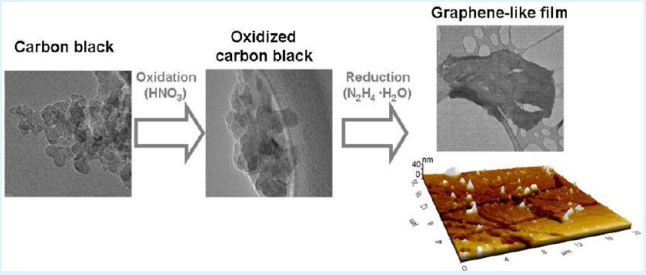

KEYWORDS: *carbon black, oxidation, hydrazine, graphene-like film*

1. INTRODUCTION

Graphene is a single-layer graphite with unusual physical, chemical, and mechanical properties.[1−8] Graphene is largely used to fabricate simple electronic devices, and it is an excellent candidate for the fabrication of electronic and optoelectronic devices. In particular, the graphene-based window electrodes can be used in the production of solid-state dye sensitized solar cells[9] and of devices for light-emitting diode (LED) and liquid crystal technologies.[10] It is also involved in the fabrication of energy-storage materials[11] and mechanical resonators.[12] Graphene can be used as channel material for the next generation of field emission transistors (FET) or as conductive sheet upon which nanometer scale devices may be patterned to create single electron or few electron transistors.[13] Graphene is also used as nanofiller in the production of polymeric nanocomposites with improved functional features.[14]

The bottleneck in the graphene-based technology is its production on a large scale. Various approaches have been used to produce graphene including one-step graphite exfoliation,[15] chemical vapor deposition (CVD) of methane gas,[16] graphite stamping,[17] graphite oxide reduction,[18] and carbon nanotube unzipping.[19] Among these, the production of graphite oxide (GO) from graphite powder and its further reduction (through chemical,[18,20] thermal,[21,22] or ultraviolet-assisted reduction[23] methods) to graphene-like material is a convenient and economic way of graphene-like sheet fabrication.

In this work, a method to produce graphene-like films starting from water suspension of oxidized carbon black (CB) is proposed. CB is largely constituted of hydrophobic material organized, at nanoscale level, in graphene layers with various degree of deviation from planarity[24,25] and a different amount of less organized areas (i.e., amorphous and disordered carbons) that makes CB particles more reactive than graphite. The selected oxidative treatment provides the partial demolition of the CB microstructure and the functionalization at the edge of the basal planes of the graphitic layers,[26] and not on them. In this way, differently from GO, the oxidized CB preserve the original graphitic network useful for the conductivity and electronic properties. The method offers scalability and potential high-volume production of graphene-like films at reduced costs.

2. EXPERIMENTAL METHODS

Materials. CB was purchased from Phillips Petroleum Co. and classified as N110 (corresponding to aggregates of rounded primary particles with a diameter of 10−15 nm) carbon black (furnace carbon black), according to ASTM classification. Its density at 25 °C is 1.8 g/mL and the specific BET area is 151 m^2/g. Nitric acid (67 wt %), sodium hydroxide (pellets), hydrochloric acid (35 wt %), thionin acetate (THA) salt (powder), ammonium hydroxide solution (28% NH_3 in H_2O), hydrazine hydrate (50%) were purchased from Sigma Aldrich (ACS grade) and used as received.

Received: January 23, 2012
Accepted: August 14, 2012
Published: August 14, 2012

   dx.doi.org/10.1021/am301197q | *ACS Appl. Mater. Interfaces* 2012, 4, 4491−4498

Characterization of the Raw CB. CB is arranged in chainlike aggregates of spherical primary particles, as shown by transmission electron microscopy (TEM).[27] The particle average diameter is 15−20 nm, with a narrow size distribution. The nanoscale organization of carbon black primary particles is typical of a disordered carbon. More organized regions are observed with a concentric organization of the stacked graphitic layers extending throughout each primary particle. H/C atomic ratio is 0.058 and the temperature of the maximum combustion rate is 690 °C.

The hydrodynamic diameter of each CB aggregate is narrow (120 ± 20 nm) as confirmed by dynamic light scattering (DLS) performed on CB suspension in N-methylpirrolidinone (NMP), a solvent very effective for the coal extraction.[28] Ultrafiltration of NMP suspension on 0.020 μm filter unit (Anotop 25, Whatman) confirmed the absence of molecules strongly absorbed on the CB surface.

Sample Preparation and Purification. CB was oxidized according to the procedure reported by Kamegawa.[29] The CB powder (500 mg) was treated with 10 mL of nitric acid (67 wt %) in a round-bottom flask at 100 °C under stirring for 90 h. After cooling at room temperature, the aqueous suspension was centrifuged (3500 rpm, 30 min) obtaining an acid-soluble fraction (AS) and an acid-insoluble fraction (AI). The AS fraction, containing mostly unreacted acid and hexacarboxylic acid (mellitic acid), was discarded. The AI was washed with distilled water (100 mL) and recovered after centrifugation (3000 rpm, 30 min). This purification step was repeated until acid traces were successfully removed. The product had a dark brown appearance and it was not as opaque black as the pristine CB. The hydrophilic product was dried at atmospheric pressure at 100 °C and labeled as HNP90. Following purification, the HNP90 sample was carefully characterized.

The reduction of HNP90 was performed by applying the procedure with hydrazine hydrate proposed for GO by Stankovich 2007.[18] In GO treatment, the reduction is an essential step in order to transform it back into a conductive graphitic material as a consequence of the partial restoration of the graphitic structure. The solution route through chemical reduction with hydrazine is the more advantageous one because a large amount of GO in the solution phase can be easily converted to graphene-like nanosheets through the partial removal of oxygenated functional groups present in the structure of GO.[30,31] We adopted a similar procedure for CB.

The HNP90 powder (20 mg) was suspended in 20 mL of distilled water in a 50 mL round-bottom flask yielding a homogeneous dark brown dispersion. The dispersion was treated with 450 μL of hydrazine hydrate (50%). The dispersion was heated in an oil bath at 100 °C under reflux for 24 h applying a constant stirring. At the end of the reaction the excess of hydrazine was neutralized with nitric acid (4 M) and the resulting black solid recovered by centrifugation (3000 rpm, 30 min).To remove traces of reagents and acid, the solid was washed with distilled water and recovered by centrifugation three times. The product was dried at atmospheric pressure at 100 °C and labeled as HNP90R. The dried HNP90R was insoluble in water and in the most common organic solvents, both polar and apolar (water, ethanol, NMP, dichloromethane, heptane, dimetilformammide). This was attributed to an increase in hydrophobicity of the material caused by a decrease in the polar functionalities on the surface and consequent intimate self-assembling interaction between the restored graphitic planes. For this reason the preparation of the film for investigation by atomic force microscope (AFM) was performed allowing a drop of the HNP90R sample drying directly on the mica plate.

Characterization. H/C atomic ratio of CB and HNP materials were measured by a Perkin−Elmer 2400 CHNSO elemental analyzer. The thermal stability of the samples was characterized by thermogravimetric analysis (TGA); all measurements were performed on a Perkin−Elmer Pyris 1 Thermogravimetric Analyzer. The carbonaceous materials were heated in oxidative environment (air, 30 mL min^{-1}) from 30 °C up to 750 °C at a rate of 10 °C min^{-1} with and without a preheating in nitrogen atmosphere (N_2, 40 mL min^{-1} from 30 °C up to 750 °C, 10 °C min^{-1}). UV−Vis spectra of CBN110 and HNP, suspended in water and ethanol, were acquired on a HP 8453 Diode Array spectrophotometer in the 200−1100 nm wavelength range by using 1 cm path-length quartz cuvette. The concentration of each suspension was 0.01 mg mL^{-1}. Fourier Transform Infrared (FTIR) spectra were recorded on a Nicolet iS10 spectrometer using the attenuated total reflectance (ATR) method. The spectra were recorded in the 400−4000 cm^{-1} range by using a germanium crystal collecting 32 scans and correcting the background noise. The experiments were performed on the powdered samples without KBr addition. The spectra were acquired and processed using the OMINIC 8 software. TEM and high-resolution electron transmission microscopy (HRTEM) images were acquired on a JEOL 2011 electron microscope operating at 200 kV using LaB_6 filament (resolution in the lattice fringe mode 0.144 nm). CB and HNP90 were dispersed by ultrasonic agitation in ethanol and placed on a carbon lacey TEM grids (20-nm thick carbon lacey coated Cu grids, Spi Supplies). The ethanol-insoluble dried HNP90R was scratched from the glass vial surface, suspended in ethanol, and placed on the TEM grid. The nanostructural organization was investigated at magnifications of 500 000×. In these images, each fringe represents the profile of a polyaromatic layer, i.e. of a graphene plane; the pixel size is 0.01384 nm. Each image was analyzed by reducing the background noise and subsequently by converting the image in a binary one. Then, the binary image was skeletonized: each fringe being one pixel-large. Each fringe can be analyzed individually by a homemade software.[32,33] Fringes shorter than an aromatic ring (i.e., 0.246 nm) were eliminated, since they do not have any physical meaning. Then, the length of all the fringes, L, i.e. the extent of the aromatic layers, was individually measured, by considering that a layer could be curved up to a distortion ratio arbitrarily fixed at 40%. Coherent domains, defined as stacks of parallel planes, also referred as BSU (basic structural units) are analyzed. The planes are considered stacked when the fringe disorientation is lower than 15% and when the interfringe distance is lower than 0.6 nm (above this value the van der Waals interactions are assumed to be negligible). The software provides the percentage of nonstacked layers (nsl) and the domain characteristics: number N of stacked layers, their diameter La and height Lc, and the mean interlayer spacing d. The error on the structural parameters depends on the pixel size (<0.15 nm in our case). The determination of surface acidic functionalities was performed according to the fluorimetric test reported by Visentin et al. for the quantification of carboxylic functionalities on carbon nanotubes.[34] The carbonaceous materials (0.01 mg) were treated with 1.5 mL of a solution of THA in ethanol (4.3×10^{-6} M) for 30 min under continuous stirring at room temperature. The suspensions were filtered on a 0.020 μm filter unit (Anotop 25, Whatman) and the fluorescence emission was measured with a Perkin-Elmer LS 50 B spectrofluorimeter. Fluorescence spectra (scan speed 100 nm/min) were recorded in the range between 570−700 nm upon excitation at 594 nm. A confocal Raman microscope (Jasco, NRS-3100) was used to obtain Raman spectra. The 514-nm line of an air-cooled Ar^+ laser (Melles Griot, 35 LAP 431−220) was injected into an integrated Olympus microscope and focused to a spot size of approximately 1 μm by a 100x objective with a final 2.0 mW power at the sample. A holographic notch filter was used to reject the excitation laser line. The Raman backscattering was collected at 180°, using a 0.1 mm slit and a diffraction lattice of 1200 grooves/mm, corresponding to an average spectral resolution of 7 cm^{-1}. It takes 200 s to collect a complete data set by a Peltier-cooled 1024 × 128 pixel CCD photon detector (Andor DU401BVI). Wavelength calibration has been performed by using cyclohexane as a standard.

Samples for AFM imaging were prepared by drop-casting the HNP90R dispersions onto freshly cleaved mica substrates (grade V-1, Electron Microscopy Sciences), which were then allowed to dry in air. AFM images were taken by means of an XE100 Park instrument operating in noncontact mode (amplitude modulation, silicon nitride cantilever from Nanosensor) at room temperature and in ambient conditions. AFM morphological characterization provided an estimation of the film thickness as well as of the surface roughness, as described below.

3. RESULTS AND DISCUSSION

Table 1 reports the elemental composition of CB and HNP. The HNP90 mass yield is 55% indicating a severe attack to the carbonaceous backbone with consequent oxidative degradation of the carbon black aggregates into smaller units. This tendency is confirmed by the elemental analysis. The hydrogen content tends to increase from 0.48 to 1.21 suggesting the reduction of the dimension of the graphitic basal planes. The increase of the H/C ratio from 0.058 (raw CB) to 0.27 (HNP90) confirms this hypothesis. The oxidation results in the introduction of oxygenated functional groups (hydroxyl, carboxylic, carbonylic) as testified by the increase of the oxygen content from 0.6% (raw CBN) to 44% (HNP90). The increase in nitrogen from 0.04% (raw CB) to 1.12% (HNP90) as a consequence of the introduction of nitro groups is also observed.

Table 1. Composition of raw CB and HNP

	C (wt %)	H (wt %)	O (wt %)	N (wt %)	O/C
CB	98.9	0.48	0.59	0.04	0.0045
HNP90	53.6	1.21	44.1	1.12	0.62
HNP90R	52.9	1.40	39.7	6.09	0.56

The chemical reduction of HNP90 with hydrazine results in the introduction of nitrogen functionalities likely in the form of hydrazones or similar structures leading to an increase of nitrogen percentage from 1.12 (HNP90) to 6.09 (HNP90R). Is it noteworthy that the oxygenated functionalities are not completely removed upon the chemical reduction. However, it represents an expected result, because CB oxidized with nitric acid has not oxygen atoms on basal planes in the form of epoxides, but only on their edges (and the selected reduction procedure basically removes oxygen from basal planes). The H/C ratio kept nearly constant (0.27−0.32), suggesting that the size of the graphitic units remains rather unchanged.

The estimation of surface acidic site content was performed applying a sensitive and fast fluorimetric assay with THA previously reported for oxidized CNT.[34] This test is based on the electrostatic interaction between the positive charge of the THA and the negative charges of the acidic sites at the surface. The unspecific contribution caused by the hydrophobic interaction between the aromatic structure of the THA and the graphitic network of the carbonaceous material was also taken into account by performing the fluorimetric test on the raw CB. The number of acid groups was estimated to be 1.7×10^{-7} mol_{COOH}/mg.

ATR-FTIR spectra of HNP90, HNP90R, and raw CB are reported in Figure 1. Spectra are baseline corrected and shifted for clarity. The spectra are broad in shape as a consequence of the presence of a complex carbon network. The most characteristic feature of HNP is the progressive increase of the intensity of the bands attributed to different types of oxygenated functionalities that are completely absent in the raw CB spectrum. The HNP90 spectrum exhibits a broad band in the 3000−3700 cm^{-1} range (O−H stretching vibrations due to carboxylic, phenolic groups and possible adsorbed H_2O). The HNP90R presents a band shift toward lower wavenumbers as a consequence of the N−H stretching band due to the introduction of NH_2 functionalities (hydrazones). Both HNP90 and HNP90R exhibit bands at 1650−1750 cm^{-1} (C═O stretching vibrations from carbonyl and carboxylic groups), 1500−1600 cm^{-1} (skeletal vibration of the sp^2 graphitic domains). The intensity of the C═O stretching band is significantly lower in the HNP90R as a consequence of the removal of carboxylic-carbonylic functionalities upon the reductive treatment. The HNP90 spectrum presents an enhanced broad band in the 1300−1100 cm^{-1} region ascribable to the overlapping of C−OH and C−O stretching vibrations (possible hydroxyls, carboxyls, oxolan-2-ones, peroxides, ethers, ketones, pyran-2,3-diones, lactols, anhydrides, benzoquinones).[35,36] The reductive treatment also reduces the intensity of the C−O broad band. The presence of nitrogen atoms in the form of nitro groups was certified with the typical bands at 1560 and 1350 cm^{-1} originated by the $-NO_2$ stretching vibrations.[37−39]

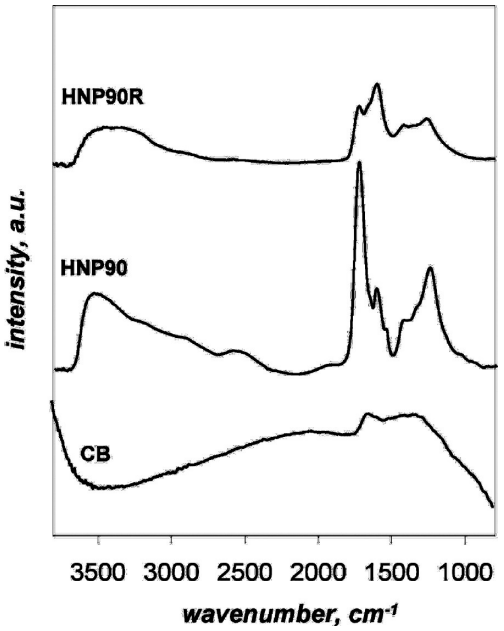

Figure 1. ATR-IR spectra of raw CB, HNP90, and HNP90R spectra (700−3800 cm^{-1}).

To get insights about the identity of the oxygenated functional groups, HNP90 and HNP90R have been treated with excess of NH_4OH (28% NH_3 in H_2O) for 30 min, after which the samples were recovered and dried. The ATR spectrum of the resulting HNP90 ammonium-salt (Figure 2a) presents bands characteristic for carboxylate ion near 1540 and 1615 cm^{-1} (asymmetrical stretching) and 1440−1360 cm^{-1} (symmetrical stretching) in addition to a broad ammonium band in the 2700−2200 cm^{-1} and to the disappearance of the O−H stretching band (not shown).[40] The HNP90 ammonium-salt partially retains the C═O stretching band (1650−1750 cm^{-1}) suggesting that functional groups other than COOH, anhydride or lactone (the latter two, via alkaline hydrolysis, would also give carboxylates) must also be present on the HNP surface which can be interpreted as single ketones or quinones.[35]

The decrease of the intensity of the C═O stretching band (1650−1750 cm^{-1}) in the HNP90R ammonium-salt spectrum (Figure 2b) suggests the presence of unreacted COOH, anhydride or lactone as well as single ketones or quinones.[35]

TGA, performed in air after preheating in nitrogen atmosphere up to 750 °C (Figure 3a) or without such preheating (Figure 3b), provides information about the thermal stability of the materials, which can be also related to their chemistry. The preheating in nitrogen atmosphere was performed with the aim to decompose the functional groups;

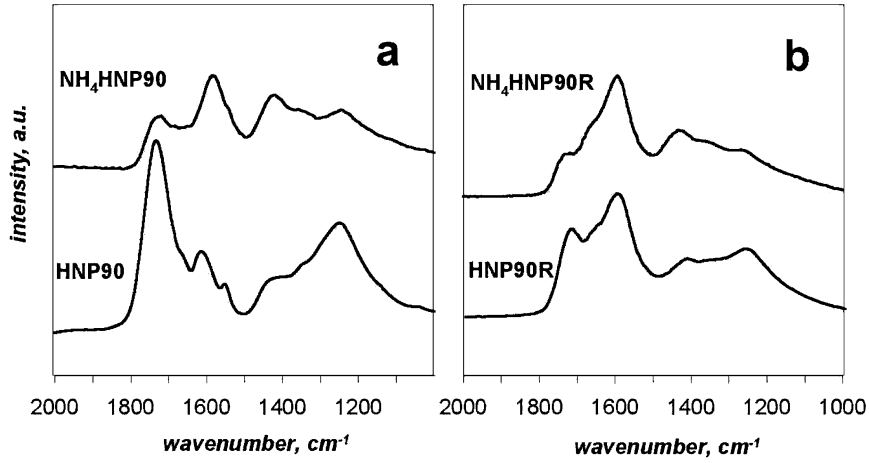

Figure 2. ATR-FTIR spectra of (a) HNP90 and (b) HPN90R together with the corresponding ammonium salt in the 1000−2000 cm^{-1} region.

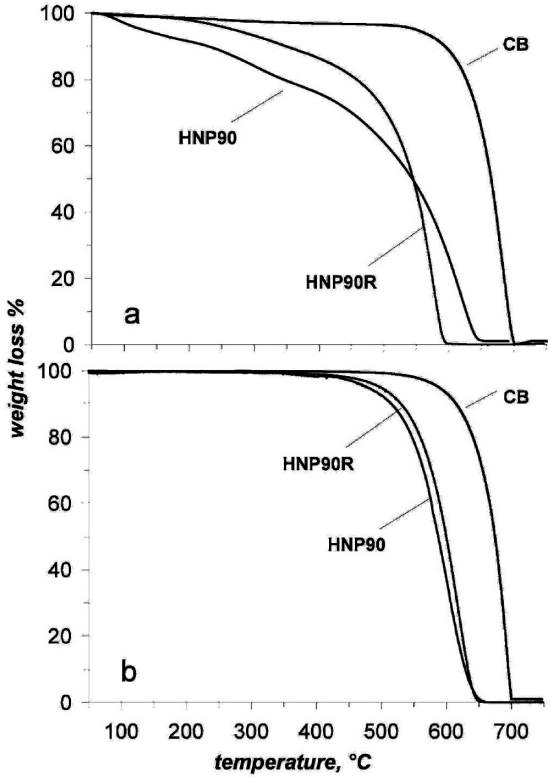

Figure 3. TGA performed in air of pristine CB, HNP90, and HNP90R, (a) without any preheating and (b) after preheating up to 750 °C in nitrogen atmosphere.

the subsequent TG in air allows to obtain information on the temperature oxidation of the graphitic core.

TGA plots of HNP90 and HNP90R in oxidative environment (air, Figure 3a) showed two low-temperature weight losses occurring at about 100 °C (10% weight loss) and between 150 and 500 °C (20−40% weight loss). The first one corresponds to the removal of physically adsorbed water. The second weight loss represents the decomposition of more stable oxygen functionalities as observed in graphite oxide.[35] The mass loss at 150−500 °C is lower in the HNP90R sample as a consequence of the lower number of oxygenated functionalities, partially removed upon chemical reduction. The high temperature mass loss corresponding to the bulk oxidation of HNP occurs at lower temperature with respect to the pristine CB (690 °C) confirming the degradation of the graphitic backbone upon the wet oxidative treatment. The TGA analysis performed in air after heating in N_2 at 750 °C (Figure 3b) showed that the sample oxidation occurs also in this case at lower temperature with respect to raw CB confirming the degradation of the pristine CB structure. It is noteworthy that the bulk oxidation of HNP90 and HNP90R are comparable suggesting a similar size of the graphitic core.

A detailed spectroscopic study of the chemical evolution of the HNP90 and HNP90R surface functional groups upon thermal treatments has been also performed. The HNP were heated in a N_2 atmosphere up to 450 and 750 °C, recovered and analyzed by ATR-IR. The ATR spectra, reported in Figure 4, confirm a progressive removal of the carbonylic/carboxylic moieties.

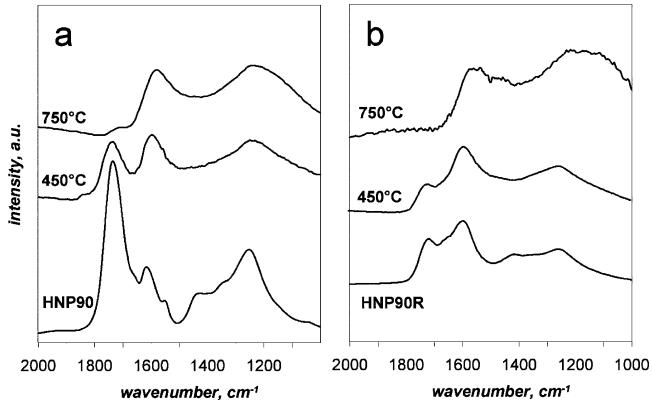

Figure 4. ATR-IR spectra in the 1000−2200 cm^{-1} region of (a) HNP90 and (b) HNP90R after heating at 450 and 750 °C in nitrogen atmosphere.

The UV−vis spectra of HNP90 and HNP90R in water dispersion are reported in Figure 5. Due to the insolubility of HNP90R, the UV−vis spectrum was taken diluting directly the wet HNP90R as recovered after the purification steps. The raw CB spectrum in ethanol suspension is also reported for comparison. The HNP90 and HNP90R samples exhibit similar broad band features suggesting that the materials present a comparable conjugation degree. The HNP90 and HNP90R maximum absorption wavelength is located around 225 nm,

dx.doi.org/10.1021/am301197q | ACS Appl. Mater. Interfaces 2012, 4, 4491−4498

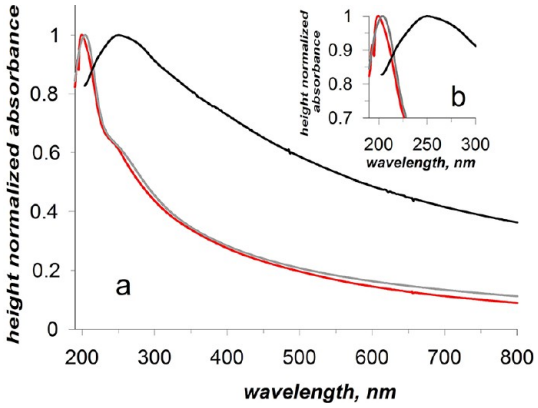

Figure 5. Height normalized UV−visible spectra of HNP90 (red), HNP90R (grey) water dispersion together with the raw CB in ethanol dispersion (black).

blue-shifted compared to that of the pristine CB (255 nm) indicating a decrease in the size of the π conjugation domains. The decrease in the size of the π conjugation domains is also confirmed by the lowering of the absorption in the visible region with respect to the pristine CB. It is noteworthy that the maximum absorption peak of HNP90R is not red-shifted with respect to the HNP90 as observed in the regular graphite oxide.[41,42] In the case of GO, the shift can be interpreted as reflecting the progressive increase of sp^2 character (aromaticity increase) as a consequence of the removal of the functional groups located on the basal layers (mainly epoxides). The preservation of the graphitic network in HNP90 and reduced HNP90, testified by the similarity in the UV−visible shape can be ascribed to a negligible functionalization at the basal plane of the HNP90 material.

The HNP90 and HNP90R microstructure and nanostructure are reported in Figure 6 together with the pristine CB. TEM images of HNP90 (Figure 6b, e) show that the carbonaceous backbone of the raw CB (Figure 6a, d) is destroyed upon the oxidative treatment. The CB nanostructure arrangement consisting of a concentric organization of the graphitic layers (Figure 6d) is not preserved in the HNP90. The HNP90R images are obtained allowing the HNP90R to dry on a flat glass surface and then scratching the resulting solid thin film. The recovered thin film was suspended in ethanol and placed on the TEM grid. The HNP90R sample (Figure 6c) consists in large flat areas that are a few layers thick, as the result of HNP90R self-assembling processes after drying.

In Figure 7 are reported the structural parameters obtained by lattice fringe analysis. L corresponds to the mean fringe length and has been evaluated by considering all the fringes larger than the size of one aromatic ring (L > 0.246 nm) and all the fringes larger than the size of two fused aromatic rings (L >

	HNP90	HNP90R
L (>0.25, θ = 40%)	0.54	0.48
L (>0.49, θ = 40%)	0.80	0.72
La (>0.25, θ = 15%)	0.38	0.31
d (>0.25, θ = 15%)	0.38	0.38
N (>0.25, θ = 15%)	2.60	2.30
Lc (>0.25, θ = 15%)	0.63	0.50
% nsl	66.5%	51.5%

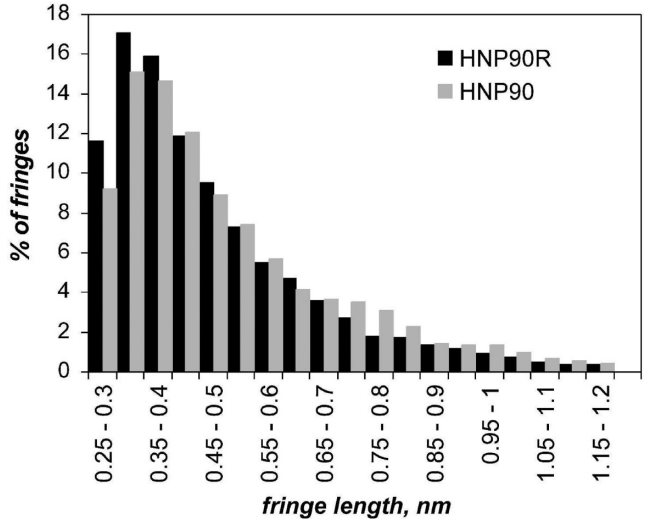

Figure 7. Structural parameters (lengths are reported in nm) and histograms of the fringe length L (admitting 40% of fringe tortuosity, L > 0.246 nm) obtained by HR-TEM image analysis of HNP90 and HNP90R.

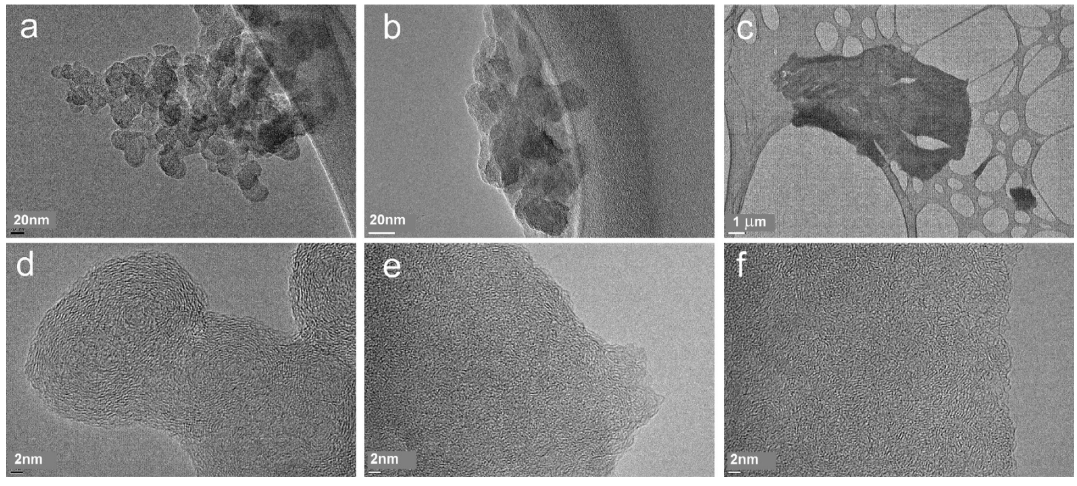

Figure 6. TEM and HRTEM images of (a, d) raw CB, (b, e) HNP90, and (c, f) HNP90R.

dx.doi.org/10.1021/am301197q | ACS Appl. Mater. Interfaces 2012, 4, 4491−4498

0.49 nm), La corresponds to the diameter and Lc corresponds to the height of the coherent domains (BSU) formed by N stacked layers with an interlayer spacing of d. The BSU structural parameters represent the mean values evaluated on 15−20 images representative of the whole sample. The histograms of the fringe lengths L for HNP90 and HNP90R, evaluated admitting a 40% of fringe tortuosity and considering all the fringes larger than the size of one aromatic ring ($L >$ 0.246 nm), are also reported in Figure 7. The interlayer spacing, d, typical of poorly ordered carbons (0.38 nm in comparison with the 0.3354 nm graphite value), is almost the same for the two samples.

Although HNP90R appears to be well structured at a nanoscale level (Figure 6c), the lattice fringe analysis reveals that the BSU parameters of the HNP90R sample are smaller with respect those obtained from the analysis of the HNP90 sample indicating a decrease in the average size of the sp^2 domains upon reduction. The HNP90R exhibits few fringes beyond 0.75 nm in length (Figure 7) with respect to HNP90. This reveals its poor graphene layer extent and organization (the layers are frequently nonstacked and only a very little number of layers are stacked). It is noteworthy that the decrease in the percentage of non stacked layers (% nsl) for HNP90R sample indicates a higher density of BSU with respect to the HNP90 sample. This result can be explained supposing the creation of new graphitic domains that are smaller in size than the ones present in HNP90 before chemical reduction, but in larger amount.

Raman spectra of CB, HNP90, and HNP90R samples are reported in Figure 8. The spectra are baseline corrected. They

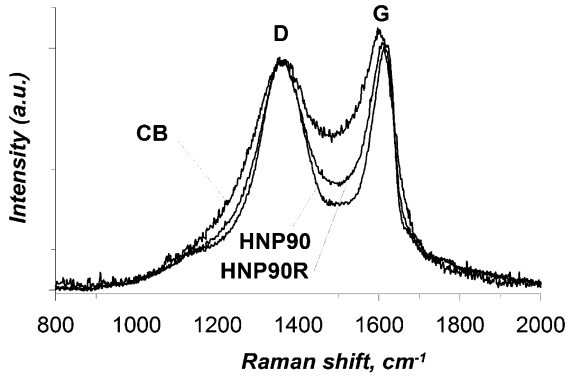

Figure 8. Raman spectra of CB, HNP90, and HNP90R recorded using 514 nm laser excitation.

exhibit the typical features of carbon-based materials with first-order G and D peaks arising at around 1580 and 1350 cm^{-1}. In all cases the comparable intensity of D and G peaks, as well as their large bandwidth (110 cm^{-1} for D-peak and 70−80 cm^{-1} for G-peak), are indicative of significant structural disorder. It is well-assessed that the area ratio of the D and G bands is a measure of the size of sp^2 ring clusters in a network of sp^3 and sp^2 bonded carbon.[43,44] The variation of the sp^2 ring clusters after the reductive procedure affects the D/G ratio in a variable way. For GO, it has been reported a variety of behaviors of the D/G ratio as a consequence of the reduction process: an increase, a decrease, a constancy or a decrease following an increase.[45] In our system, it was observed that the D-band to G-band ratio remains nearly constant before and after chemical reduction. This behavior suggests that reduction does not lead to an expansion of the original sp^2 domains as a consequence of the treatment with hydrazine, confirming the preservation of the graphitic network as observed by UV−visible spectroscopy (Figure 5).

AFM measurements provided information about the surface features of the measured HNP90R sample.

Diluted neutral solutions of HNP90R (2 mg mL^{-1}) were drop-cast onto a cleaved mica plate, evaporated at 100 °C and then mounted on the AFM scan head. The self-assembled HNP90R sample is made by pliant sheets that easily conform to any feature of that surface. The diluted sample naturally shrinks during the evaporation of the solvent. Thus, some fractures appear on the surface, likely down the mica substrate, as a result of the film drying process; their depth gives an estimation on the thickness of such dropped sample. All AFM measurements were performed in noncontact mode. Figure 9a shows a scan over an area of 20 μm × 20 μm. The surface appears characterized by the fractures mentioned above, and each portion delimited by them looks regular and flat. Indeed, the roughness on a compact region estimated by the scan profile reported in Figure 9b is about 0.5 nm peak to peak over a distance of 1 μm, and of the order of 0.1 nm if considering a root-mean-square roughness. These values clearly indicate flatness at atomic level. The same profile, crossing a fractured part of the surface, shows that the height of the resulting islands is about 20 nm. These results were common to the whole investigated surface, suggesting that several single sheets assemble on each other on the different terraces. Typically, the thicknesses of a graphene-like monolayer obtained by chemical reduction of GO is in the range of 0.6−0.8 nm[46] so the shown film most likely consists of about 25 layers. Such a conclusion could be confirmed by measuring the height differences between adjacent flat regions, that can be ascribed to the different number of concurring sheets; even better, the superposition of different layers can be inferred through the scan profile reported in Figure 9c; this line crosses a small nonflat portion on a terrace, originated by a nonregular edge of some sheets. The resulting profile puts in evidence the presence of height discontinuity between the exposed flat surfaces. Some circular-like particles appears on the surface. We attribute them to the presence of some moisture and impurities coming from the solution or from the environment. Of course, we cannot exclude that they can be originated by spurious phases arising during the assembling; however, their height is comparable with the total thickness of the film, and this circumstance supports our first hypothesis. As concerns the thickness of the film, we can suppose that it is strongly dependent on the HNP90R concentration in the water solution before the drying; this issue will be argument for further work.

Figure 9d is a 3D representation of the surface, which provides global information about height values of the different imaged structures. The resulting distribution of the measured relative heights gives the histogram reported in Figure 9e. In this plot, the central part is representative of the flat terraces, and its spread must be ascribed to the different number of sheets. The two tails at lower and higher height values are instead originated by the depth inside the fractures and by the circular particles on the surfaces respectively. In addition, a quantitative evaluation of the in-plane features shows a particular "geometric" occurrence. In Figure 9f some lines are drawn along the surface discontinuities. Interestingly, the angles between such lines are near 60 and 120°: the crystal orientation is reproduced on a macroscopic scale, resulting in weak lines

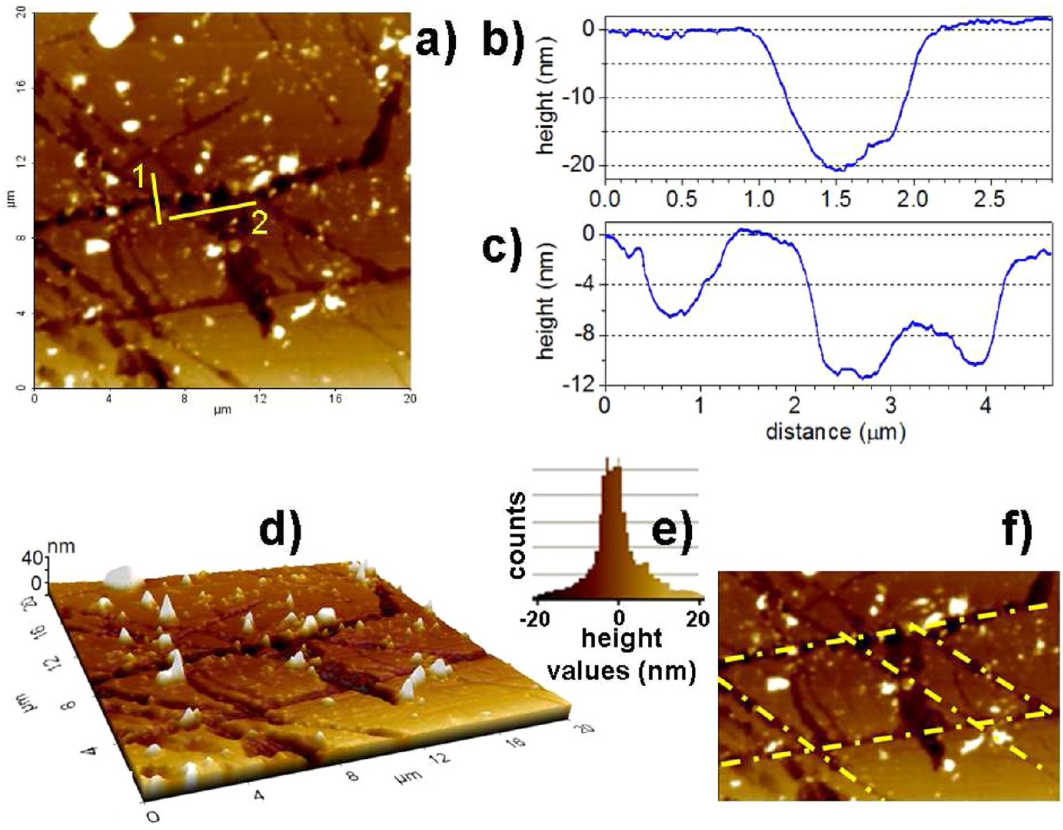

Figure 9. (a) Noncontact AFM topographic image on the HNP90R, 20 μm × 20 μm; (b, c) two height profiles, along lines (b) 1 and (c) 2 in the image, respectively. (d) 3D representation of the image in a, showing the height of the circular features and pointing out their spurious nature. (e) Histogram of the height values over the whole image. (f) Highlights of the fracture lines and of the relative angles.

along which the surface discontinuity occurs with higher probability than elsewhere. This phenomenon is a strong confirmation of the single-layer nature of the observed terraces and, on the other side, shows the presence of a size-scalability of microscopic lattice features.

Basic electrical characterization shows the effect of the reduction on the transport properties. Current vs voltage (I–V) measurements have been carried out in a four contact geometry. Pristine CB and the oxidized one (sample HPN90) did not reveal any electrical current within the sensitivity of our experimental apparatus (Keithley picoammeter model 6485) up to an applied voltage of 10 V. On the contrary, on the reduced CB film (sample HPN90R) we observed an ohmic behavior of the I–V characteristic (Figure 10). The resistivity can be evaluated by following the Van der Pauw method[47] and assuming for the thickness the value estimated by AFM measurements, obtaining a value of 6 Ω m. This value, however, likely represents an overestimation of the intrinsic resistivity of the material of the film, since the fragmentation of the sample on the micrometer scale leads to a decrease of the effective circulating current for a given voltage in a given geometry.

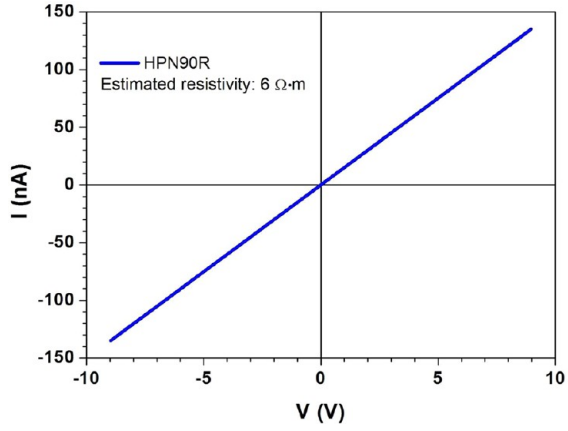

Figure 10. I–V characteristic of HPN90R, measured in a four contact geometry.

4. CONCLUSIONS

The reported approach for producing graphene-like thin film has significant advantages over the conventional method based on graphite oxidation and reduction. Graphene-like layers were produced in mild conditions with high yields and does not involve the use of hydrazine vapor for the restoring of the graphitic network. Moreover all procedures are performed in aqueous environments, which is environmentally advantageous and highly compatible to an industrial scale-up process. This approach provides promising capability for manipulating the physical properties of thin films, including controllability of film thickness (under study), sheet resistance, and light transparency, and thus, it is anticipated to be useful in various electrical, optical, and biological applications. The potential application of self-assembling graphene-like layers for facing non planar substrates is currently under study.

AUTHOR INFORMATION

Corresponding Author
*E-mail: alfe@irc.cnr.it

Notes
The authors declare no competing financial interest.

ACKNOWLEDGMENTS

The research leading to these results has received funding from the Accordo CNR-MSE "Carbone Pulito-CO_2 capture", NIPS (Nanoparticle Impact on Pulmonary Surfactant Interfacial Properties) – Seed Project 2009– IIT and the European Union Seventh Framework Programme (FP7/2007-2013) under Grant 264098–MAMA.

REFERENCES

(1) Novoselov, K. S.; Geim, A. K.; Morozov, S. V.; Jiang, D.; Zhang, Y.; Dubonos, S. V.; Grigorieva, I. V.; Firsov, A. A. *Science* **2004**, *306*, 666–669.
(2) Allen, M. J.; Tung, V. C.; Kaner, R. B. *Chem. Rev.* **2010**, *110*, 132–145.
(3) Balandin, A. A.; Ghosh, S.; Bao, W.; Calizo, I.; Teweldebrhan, D.; Miao, F.; Lau, C. N. *Nano Lett.* **2008**, *8* (3), 902–907.
(4) Bolotin, K. I.; Sikes, K. J.; Jiang, Z.; Klima, M.; Fudenberg, G.; Hone, J.; Kim, P.; Stormer, H. L. *Solid State Commun.* **2008**, *146*, 351–355.
(5) Wang, X.; Zhi, L.; Müllen, K. *Nano Lett.* **2008**, *8* (1), 323–327.
(6) Novoselov, K. S.; Geim, A. K.; Morozov, S. V.; Jiang, D.; Katsnelson, M. I.; Grigorieva, I. V.; Dubonos, S. V.; Firvos, A. A. *Nature* **2005**, *438*, 197–200.
(7) Zhang, Y.; Tan, Y. W.; Stormer, H. L.; Kim, P. *Nature* **2005**, *428*, 201–204.
(8) Lee, C.; Wei, X.; Kysar, J. W.; Hone, J. *Science* **2008**, *321*, 385–388.
(9) Choi, H.; Kim, H.; Hwang, S.; Choi, W.; Jeon, M. *Sol. Energy Mater. Sol. Cells* **2010**, *95*, 323–325.
(10) Blake, P.; Brimicombe, P. D.; Nair, R. R.; Booth, T. J.; Jiang, D.; Schedin, F.; Ponomarenko, L. A.; Morozov, S. V.; Gleeson, H. F.; Hill, E. W.; Geim, A. K.; Novoselov, K. S. *Nano Lett.* **2008**, *8* (6), 1704–1708.
(11) Stoller, M. D.; Park, S.; Zhu, Y.; An, J.; Ruoff, R. S. *Nano Lett.* **2008**, *8*, 3498–3502.
(12) Bunch, J. S.; van der Zande, A. M.; Verbridge, S. S.; Frank, I. W.; Tanenbaum, D. M.; Parpia, J. M.; Craighead, H. G.; McEuen, P. L. *Science* **2007**, *315*, 490–493.
(13) Geim, A. K.; Novoselov, K. S. *Nat. Mater.* **2007**, *6* (3), 183–191.
(14) T. Ramanathan, T.; Abdala, A. A.; Stankovich, S.; Dikin, D. A.; M. Herrera-Alonso, M.; Piner, R. D.; Adamson, D. H.; Schniepp, H. C.; Chen, X.; Ruoff, R. S.; Nguyen, S. T.; Aksay, I. A.; Prud'Homme, R. K.; Brinson, L. C. *Nat. Nanotechnol.* **2008**, *3*, 327–331.
(15) Lee, J. H.; Shin, D. W.; Makotchenko, V. G.; Nazarov, A. S.; Fedorov, V. E.; Kim, Y. H.; Choi, J. Y.; Kim, J. M.; Yoo, J. B. *Adv. Mater.* **2009**, *21*, 4383–4387.
(16) Kim, K. S.; Zhao, Y.; Jang, H.; Lee, S. Y.; Kim, J. M.; Kim, K. S.; Ahn, J. H.; Kim, P.; Choi, J. H.; Hong, B. H. *Nature* **2009**, *457*, 706–710.
(17) Li, D. S.; Windl, W.; Padture, N. P. *Adv. Mater.* **2009**, *21*, 1243–1246.
(18) Stankovich, S.; Dikin, D. A.; Piner, R. D.; Kohlhaas, K. A.; Kleinhammens, A.; Jia, Y.; Wu, Y.; Nguyen, S. T.; Ruoff, R. S. *Carbon* **2007**, *45*, 1558–1565.
(19) Jiao, L. Y.; Zhang, L.; Wang, X. R.; Diankov, G.; Dai, H. J. *Nature* **2009**, *458*, 877–880.
(20) Luo, D.; Zhang, G.; Liu, J.; Sun, X. *J. Phys. Chem. C* **2011**, *115*, 11327–11335.
(21) Schniepp, H. C.; Li, J. L.; McAllister, M. J.; Sai, H.; Herrera-Alonso, M.; Adamson, D. H.; Prud'homme, R. K.; Car, R.; Saville, D. A.; Aksay, I. A. *J. Phys. Chem. B* **2006**, *110*, 8535–8539.
(22) Liao, K. H.; Mittal, A.; Bose, S.; Leighton, C.; Mkhoyan, K. A.; Macosko, C. W. *ACS Nano* **2011**, *5* (2), 1253–1258.
(23) Williams, G.; Seger, B.; Kamat, P. V. *ACS Nano* **2008**, *2*, 1487–1491.
(24) Kinoshita, K. *Carbon-Electrochemical and Physicochemical Properties*; Wiley: New York, 1988.
(25) Donnet, J. B.; Bansal, R. C.; Wang, M. J. *Carbon Black: Science and Technology*, 2nd ed.; Dekker: New York, 1993.
(26) Kamegawa, K.; Nisiukubo, K.; Kodama, M.; Adachi, Y.; Yoshida, H. *Carbon* **2002**, *40*, 1447–1455.
(27) Santini, E.; Ravera, F.; Ferrari, M.; Alfè, M.; Ciajolo, A.; Liggieri, L. *Colloids Surf., A* **2010**, *365*, 189–198.
(28) Shui, H. *Fuel* **2005**, *84*, 939–941.
(29) Kamegawa, K.; Nisiukubo, K.; Yoshida, H. *Carbon* **1998**, *36* (4), 433–441.
(30) Ren, P. G.; Yan, D. X.; Ji, X.; Chen, T.; Li, Z. M. *Nanotechnology* **2011**, *22*, 055705.
(31) Moon, I. K.; Lee, J.; Lee, H. *Chem. Commun.* **2011**, *47*, 9681–9683.
(32) Shim, H. S.; Hurt, R.; Yang, N. *Carbon* **2000**, *38*, 29–45.
(33) Galvez, A.; Herlin-Boime, M.; Reynaud, C.; Clinard, C.; Rouzaud, J. N. *Carbon* **2002**, *40*, 2775–2789.
(34) Visentin, S.; Barbero, N.; Musso, S.; Mussi, V.; Biale, C.; Ploeger, R.; Viscardi, G. *Chem. Commun.* **2010**, *46*, 1443–1445.
(35) Acik, M.; Mattevi, C.; Gong, C.; Lee, G.; Cho, K.; Chhowalla, M.; Chabal, Y. J. *ACS Nano* **2010**, *4* (10), 5861–5868.
(36) Titelman, G. I.; Gelman, V.; Bron, S.; Khalfin, R. L.; Cohen, Y.; Bianco-Peled, H. *Carbon* **2005**, *43*, 641–649.
(37) Meldrum, B. J.; Rochester, C. H. *J Chem. Soc., Faraday Trans.* **1990**, *86*, 861–865.
(38) Akhter, M. S.; Chughtai, A. R.; Smith, D. M. *J. Phys. Chem.* **1984**, *88*, 5334–5342.
(39) Zawadzki, J. *Carbon* **1980**, *18*, 281–285.
(40) Silverstein, M.; Webster, F. X.; Kiemle, D. *Spectrometric Identification of Organic Compounds*, fourth ed.; Wiley: New York, 2008.
(41) Li, D.; Muller, M. B.; Gilje, S.; Kaner, R. B.; Wallace, G. G. *Nat. Nanotechnol.* **2008**, *3*, 101–105.
(42) Luo, L.; Cote, L. J.; Tung, V. C.; Tan, A. T. L.; Goins, P. E.; Wu, J.; Huang, J. *J. Am. Chem. Soc.* **2010**, *132* (50), 17667–17669.
(43) Ferrari, A. C.; Robertson, J. *Philos. Trans. R. Soc. Lond. Ser. A-Math. Phys. Eng. Sci.* **2004**, *362*, 2477–2512.
(44) Pimenta, M. A.; Dresselhaus, G.; Dresselhaus, M. S.; Cancado, L. G.; Jorio, A.; Saito, R. *Phys. Chem. Chem. Phys.* **2007**, *9*, 1276–1290.
(45) Eda, G.; Chhowalla, M. *Adv. Mater.* **2010**, *22*, 2392–2415.
(46) Paredes, J. I.; Villar-Rodil, S.; Solıs-Fernandez, P.; Martınez-Alonso, A.; Tascon, J. M. D. *Langmuir* **2009**, *25* (10), 5957–5968.
(47) Van der Pauw, L. J. *Philips Res. Rep.* **1958**, *13*, 1–9.